XL CILAMCE
IBERO-LATIN AMERICAN CONGRESS ON COMPUTATIONAL METHODS IN ENGINEERING
NOVEMBER 11-14, 2019
Praiamar Natal Hotel & Convention Natal, RN-BRAZIL

MODELING CRACK PROPAGATION PROCESS IN CORTICAL BONE MICROSTRUCTURE

Marcos André Margalho de Barros
Luís Antônio Guimarães Bitencourt Júnior
mbarros@usp.br
luis.bitencourt@usp.br
Polytechnic School at the University of São Paulo
Av. Prof. Almeida Prado, trav. 2, 271, Cidade Universitária, 05508 – 900, São Paulo, Brazil
Osvaldo Luís Manzoli
osvaldo.l.manzoli@unesp.br
São Paulo State University (UNESP)
Av. Luiz Edmundo C. Coube, 14-01, 17033-360, Bauru, SP, Brazil

Abstract. This work aims to simulate the crack initiation and propagation processes in cortical bone using a two-dimensional mesh fragmentation technique. High aspect ratio elements (triangle elements with height much smaller than its length) are inserted between the regular constant strain triangle finite elements, and their behavior is described by a tensile-damage model (stress-strain relation). The constitutive model is integrated using an implicit-explicit (Impl-Ex) scheme in order to avoid convergence problems. The proposed approach is applied to simulate cortical bone microstructures, described as a 4-phased material: interstitial matrix, cement line, osteon and Haversian canal. The methodology is validated through the simulation of conceptual problems available in literature, in which the influence of the cortical bone microstructure in crack propagation process is assessed in three-point bending tests, by considering the presence of one and two osteons.

Keywords: Cortical bone, Finite element method, Damage mechanics, Mesh fragmentation technique.

1 Introduction

In the last century, it has been occurring in several countries, a phenomenon known as the ageing of the population. Consequently, health problems that frequently occur on elders have had an increase in the number of incidents which, in addition to the short and long-term problems, are financially expensive for the society (Burge et al. [1]). Although the technology has been converging to the personalized medicine, there are still steps in the development stairway to accomplish such achievement (Podshivalov et al. [2]).

Bone is a living tissue that is both strong, tough and lightweight. Macroscopically, the bone can be described by two tissues: the highly mineralized cortical bone and the porous structure called trabecular bone (Junqueira and Carneiro [3]). The cortical bone is a heterogeneous hierarchical material with non-isotropic properties that needs to be studied in different length scales. In the microscale, the cortical bone is composed by the interstitial matrix, cement line, secondary osteons (it is also referred as osteons in this work) and Haversian canals (mechanically negligible). For this reason, in this scale of visualization, the bone is considered as a 4-phased composite material (Budyn and Hoc [4]; Marco et al. [5]; Gustafsson et al. [6]). In summary, the osteons can be described as stiff fibers embedded within a stiff matrix separated by a thin layer (cement line) which is known to act as a crack amplifier. Notwithstanding the scientific consensus on the matrix and osteons mechanical properties, the cement line properties are still in discussion (Skedros et al. [7]; Milovanovic et al. [8]; Nobakhti et al. [9]). In this work the cement line is considered as a much less stiff material than the osteons and matrix.

The finite element method has been demonstrated as a valuable tool to assess cortical bone microstructure mechanical behavior since the 70s (Brekelmans et al. [10]; Huiskes and Chao [11]; Duda et al. [12]; Bessho et al. [13]; Zysset et al. [14]). The computational resource availability in the last decades has allowed complex finite element analyses to be carried out, including several non-linear analyses simulating crack propagation on microstructure models (Li et al. [15]; Gustafsson et al. [16]]). These works aimed to reproduce the behavior observed in experimental researches, in which the crack initiation and propagation in bones are dictated by the osteon distribution in the matrix. In addition, the cracks are known to travel through the matrix and tend to go around the osteons due to the interface properties (Burr et al. [17]).

Recently, the Extended Finite Element Method (XFEM) has been widely used to simulate the nonlinear behavior of the cortical bone microstructure (Abdel-Wahab [18]; Baptista et al. [19]). However, these numerical models usually do not have a law to capture or describe the crack initiation phenomenon, so a single predetermined crack courses through the model.

The mesh fragmentation technique, developed by Manzoli et al. [20] is based on the use of high aspect ratio finite elements proposed by Manzoli et al. [21], which are inserted in between regular constant strain triangle elements of the mesh in order to capture the nonlinear behavior of the structures. A continuum tensile-damage model is applied in these interface elements that will behave as linear material if the stress applied is below the tension strength or else will behave according to a damage evolution law. Therefore, this methodology does not require a crack initiation or crack evolution law due to the High Aspect Ratio (HAR) finite elements being interpreted as the cracks.

In this work, the mesh fragmentation technique (Manzoli et al. [20]) based on the use of high aspect ratio finite elements proposed by Manzoli et al. [21] is applied to describe the crack propagation in the cortical bone microstructure. An Impl-Ex integration scheme (proposed by Oliver et al. [22]) is used to integrate a tensile damage model, and consequently, to avoid convergence problems.

2 Numerical model

The cortical bone is a complex heterogeneous material that is organized in complex geometries. In this work, the numerical model aims to capture the mechanical behavior of this material in two-dimensional quasi-static analyses considering it as a 4-phase material (interstitial matrix, osteon,

cement line and Haversian canal).

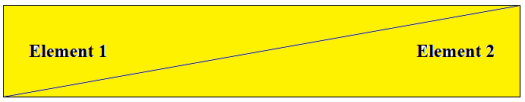

Figure 1. A pair of HAR finite elements.

The 2D numerical models are developed using the concepts of the Mesh Fragmentation Technique (MFT). Firstly, after the discretization of the problem using Constant Strain Triangle (CST) elements, a pair of High Aspect Ratio (HAR) finite elements (see Figure 1) is inserted between two adjacent CST elements.

The output file is loaded in MeFS (Mesh Fragmentation Software developed by the authors in the Matlab's App Designer environment) to insert the HAR finite elements (Figure 2), following the steps:

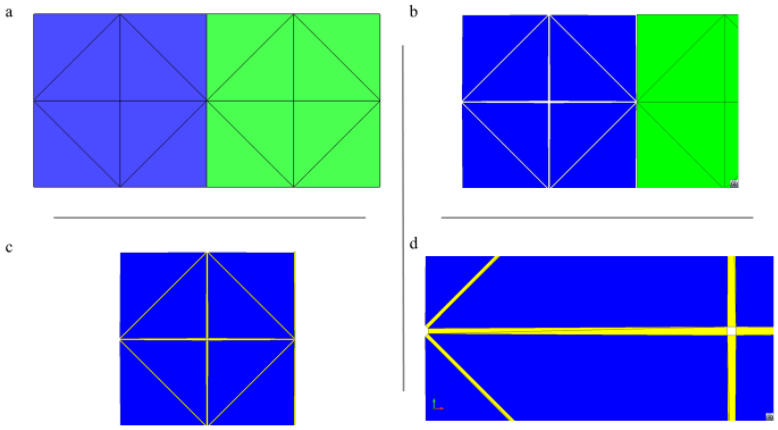

Figure 2. Detailed view of the mesh fragmentation process. In this image, the height assigned to the HARs is greater than usual to facilitate the visualization. In this example, the blue material is fragmented and the green is left intact. (a) Regular CST mesh generated in GiD; (b) Gaps are inserted between the interfaces; (c) HAR finite elements (yellow) are inserted in the gaps; (d) Details of the HAR finite elements (yellow).

- In MeFS, the information about the number of materials and the number of CST elements assigned to each phase of the composite are detailed.
- The user must define the following parameters: height of the HAR elements, scale multiplier (input required if the user wants to change the length unit of the calculation file) and the materials to be fragmented.
- After these definitions, the fragmentation process begins:
    a) The software identifies all the elements to be fragmentated and consequently their interfaces.
    b) Separation process begins. In this step, nodes are created, and the regular CSTs are separated. The distances between regular CSTs is defined by the user based on the height adopted for the HAR elements.
    c) The HAR elements are inserted to fill the gaps. The materials assigned to them are defined automatically.
    d) The output file is generated with the updated nodes and elements of the mesh.

Finally, the user updates the calculation file and loads it in the finite element solver.

2.1 HAR finite elements

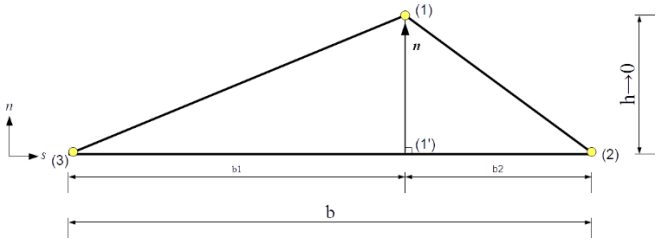

Figure 3. High aspect ratio finite element (adapted from Manzoli et al. [20]).

The three-node triangular finite element with high aspect ratio is illustrated in Figure 3. As can be seen in this figure, the base *b* is composed by the segment between nodes 2 and 3, *h* is the element height between node 1 and its projection 1'.

It is well known that using a standard finite element approximation, the strain field of a finite element can be written as:

$$\boldsymbol{\varepsilon} = \boldsymbol{B}\boldsymbol{u} \tag{1}$$

where $\boldsymbol{B}$ and $\boldsymbol{u}$ are the strain-displacement matrix and the nodal displacement vector, respectively. Adopting a Cartesian coordinate system ($\boldsymbol{n}$,$\boldsymbol{s}$) with the vector $\boldsymbol{n}$ being orthogonal to the base of element, the nodal displacement vector of the element is defined as:

$$\boldsymbol{u} = \{u_s^1, u_n^1, u_s^2, u_n^2, u_s^3, u_n^3\}^{\mathrm{T}}. \tag{2}$$

The vector $\widehat{\boldsymbol{u}}$ gathers the relative displacement between the node (1) and its projection (1'). Thus, it contains the parallel and orthogonal components:

$$\widehat{\boldsymbol{u}} = \begin{Bmatrix} \hat{u}_s^1 \\ \hat{u}_n^1 \end{Bmatrix} = \begin{Bmatrix} u_s^1 - u_s^{1'} \\ u_n^1 - u_n^{1'} \end{Bmatrix} \tag{3}$$

Substituting the geometric components *h* and *b* (height and base) from Figure 3 and the relative displacements from Eqs. (3) in (1), the strain tensor ($\boldsymbol{\varepsilon}$) can be rewritten as:

$$\boldsymbol{\varepsilon} = \begin{Bmatrix} \varepsilon_{ss} \\ \varepsilon_{nn} \\ \varepsilon_{sn} \end{Bmatrix} = \begin{Bmatrix} \dfrac{u_s^3 - u_s^2}{b} \\ \dfrac{\hat{u}_n^1}{h} \\ \dfrac{u_n^3 - u_n^2}{2b} + \dfrac{\hat{u}_s^1}{2h} \end{Bmatrix}. \tag{4}$$

The strain tensor ($\boldsymbol{\varepsilon}$) can be divided into two parts (Eq. 5), in which $\hat{\boldsymbol{\varepsilon}}$ collects the components that depends of the element's height (Eq. 6)), and $\tilde{\boldsymbol{\varepsilon}}$ contains the rest of components (Eq. 7).

$$\boldsymbol{\varepsilon} = \hat{\boldsymbol{\varepsilon}} + \tilde{\boldsymbol{\varepsilon}} \tag{5}$$

$$\hat{\boldsymbol{\varepsilon}} = \frac{1}{h}\begin{Bmatrix} 0 \\ \hat{u}_n^1 \\ \dfrac{\hat{u}_s^1}{2} \end{Bmatrix} \tag{6}$$

$$\tilde{\boldsymbol{\varepsilon}} = \frac{1}{b}\begin{Bmatrix} u_s^3 - u_s^2 \\ 0 \\ \dfrac{u_n^3 - u_n^2}{2} \end{Bmatrix}. \tag{7}$$

It is important to note that when $h \to 0$ in Eq. (5), the $\tilde{\boldsymbol{\varepsilon}}$ component (bounded) loses relevance; thus, the strain field is related almost exclusively to the $\hat{\boldsymbol{\varepsilon}}$ parcel (unbounded) as a function of $\hat{\boldsymbol{u}}$, which becomes the measure of a displacement discontinuity (strong discontinuity). This structure is analogous to the kinematics of the Continuum Strong Discontinuity Approach (CSDA) as described by Manzoli et al. [21]. Finally, based on CSDA, bounded stress can be obtained from unbounded strains by means of constitutive relation.

2.2 Tensile-damage model

In this work, a tensile-damage model is assigned to HAR elements to describe the crack initiation and propagation process. In summary, the stress (normal to the element's base) is verified: the element remains in the elastic regime if it does not reach the element's tension strength or else the damage is accounted, and the crack initiation starts.

The nominal stress is defined as:

$$\boldsymbol{\sigma} = (1 - d)\bar{\boldsymbol{\sigma}}, \tag{8}$$

where $d \in [0,1]$ is the tensile scalar damage variable, $\bar{\sigma}$ is the effective stress tensor defined by the product of the fourth order elastic tensor by the strain tensor ($\boldsymbol{C}$:$\boldsymbol{\varepsilon}$).

The elastic domain is defined by the following damage criterion:

$$\varphi = \sigma_{nn} - q(r) \leq 0, \tag{9}$$

where σ_{nn} is the nominal stress normal to the element's base and $q(r)$ is the internal stress variable which is a function of the strain-like variable (r) that is the parcel that determine the elastic regime threshold in effective stress field.

The damage criterion can be rewritten in effective stress field as:

$$\bar{\varphi} = \bar{\sigma}_{nn} - r \leq 0, \tag{10}$$

$$d = 1 - \frac{q}{r}. \tag{11}$$

The damage evolution is calculated using the Eq. (11), and the internal stress variable (q) is defined with an exponential law:

$$q(r) = r_0 e^{Ah\left(1-\frac{r}{r_0}\right)}. \tag{12}$$

The softening parameter is given by:

$$A = \frac{r_0^2}{E G_f^I}. \tag{13}$$

where E is the Young Modulus and G_f^I is the fracture energy for mode I.

Finally, the Kuhn-Tucker relations set the loading and unloading conditions:

$$\bar{\varphi} \leq 0, \;\; \dot{r} \geq 0 \text{ e } \dot{r}\bar{\varphi} = 0 \tag{14}$$

2.3 Impl-Ex integration scheme

The implicit-explicit integration scheme (Impl-Ex) proposed by Oliver et al. [22] is used for the integration of the stress-strain relation to avoid numerical convergence problems. This methodology has been used in constitutive models based on damage mechanics (Manzoli et al. [20] and Rodrigues et al. [23]).

Thus, the integration of the tensile damage model can be summarized at a current pseudo-time t_{n+1} in the following steps:

1. Input variables: $\boldsymbol{\varepsilon}_{(n+1)}, \boldsymbol{C}, r_{(n)} r_{(n-1),} r_0, A$
2. Evaluate the effective stress tensor:
$$\bar{\boldsymbol{\sigma}}_{(n+1)} = \boldsymbol{C} : \boldsymbol{\varepsilon}_{(n+1)}$$
3. Verify the loading-unloading conditions:
If $\bar{\sigma}_{nn_{(n+1)}} > r_{(n)}$: $r_{(n+1)} = \bar{\sigma}_{nn_{(n+1)}}$;
Else: $r_{(n+1)} = r_{(n)}$
4. Compute an explicit linear extrapolation of the internal strain-like variable:
$$\tilde{r}_{(n+1)} = r_{(n)} + \frac{r_{(n)} - r_{(n-1)}}{\Delta t_{(n)}} \Delta t_{(n+1)}$$
5. Evaluate the damage variable as function of the extrapolated strain-like internal variable:
$$\tilde{d}_{(n+1)} = 1 - \frac{r_0}{\tilde{r}_{(n+1)}} e^{Ah\left(1 - \frac{\tilde{r}_{(n+1)}}{r_0}\right)}$$
6. Compute the nominal stress tensor $\tilde{\boldsymbol{\sigma}}_{(n+1)}$;
If $\bar{\sigma}_{\boldsymbol{nn}_{(\boldsymbol{n})}} \leq 0$: $\tilde{\boldsymbol{\sigma}}_{(n+1)} = \bar{\boldsymbol{\sigma}}_{(n+1)}$;
Else: $\tilde{\boldsymbol{\sigma}}_{(n+1)} = (1 - \tilde{d}_{(n+1)}) \bar{\boldsymbol{\sigma}}_{(n+1)}$
7. Evaluate the effective algorithmic tangent operator $\tilde{\boldsymbol{C}}^{tang}_{(n+1)}$.
If $\bar{\sigma}_{\boldsymbol{nn}_{(\boldsymbol{n})}} \leq 0$: $\tilde{\boldsymbol{C}}^{tang}_{(n+1)} = \boldsymbol{C}$;
Else: $\tilde{\boldsymbol{C}}^{tang}_{(n+1)} = (1 - \tilde{d}_{(n+1)}) \boldsymbol{C}$
8. Output variables: $\tilde{\boldsymbol{\sigma}}_{(n+1)}, \bar{\sigma}_{\boldsymbol{nn}_{(\boldsymbol{n})}}, r_{(n+1)}, \Delta r_{(n+1)}$.

3 Numerical Analyses

3.1 Description of the numerical models

The 2D numerical models of this work represent a conceptual approximation for the cortical bone microstructure, as proposed by Marco et al. [5]. The cortical bone is assumed as a 4-phase material, and the properties assigned to each phase are listed in Table 1. The standard CST elements and undamaged HAR elements behave linearly elastic.

Table 1. Material properties adopted.

Component	Young's Modulus (MPa)	f_t (MPa)	G_c (N/m)
Secondary Osteon	13290[a]	100[b]	800[c]
Interstitial Matrix	14610[c,d]	55[e]	238[c]
Cement Line	88[f]	6[g]	163[g]

* The Haversian canal is considered as a structural void.
** [a] Vercher et al. [24]; [b] Cowin [25]; [c] Li et al. [15]; [d] Rho et al. [26]; [e] Arango Villegas [27]; [f] Nobakhti et al. [9]; [g] Giner et al. 2017 [28].
*** The Poisson's ratio is 0,3 and constant for all the components.

The numerical analyses are performed in plane strain state by considering quasi-static loading and small displacements.

Figure 4 and 5 show the setup of the three-point bending tests with one and two osteons, respectively. The displacements are imposed at the top of the beams in 5000 steps equally divided. In these models, the green color is set to identify the secondary osteons and blue to the interstitial matrix. Prior to the analyses, the HAR elements, that represent the cement line and to fill the gaps between the CST elements (mesh fragmentation process) are not visible due to their small height of 0,01μm. In the preprocessing stage, unstructured meshes were generated with 5μm and 10μm to all surfaces for

models with one and two osteons, respectively. In addition, the discretization is performed considering the size of 5μm for cement line.

It is important to highlight that all the interfaces between CST elements are fragmented. The mesh dependency of these problems is not significant provided that unstructured mesh with a reasonable refinement are used as stated by Manzoli et al. [20].

The dimensions of the one osteon model (Fig. 4) are 0,64 x 0,24mm² with an osteon diameter of 0,2mm and Haversian canal with diameter of 0,05mm.

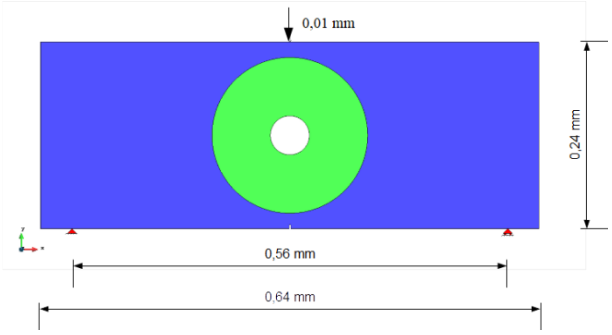

Figure 4. Setup of the one osteon bending test.

The two osteons model (Fig. 5) with 1,0 x 0,4mm² contains a large osteon with diameter of 0,2mm and Haversian canal with diameter of 0,05mm and a small osteon with a diameter of 0,12 and a Haversian canal with a diameter of 0,06mm.

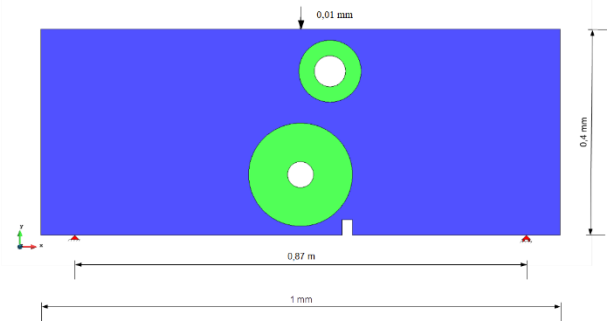

Figure 5. Setup of the two osteons bending test.

3.2 Results

The results of the two finite element analyses (FEA) are discussed in this section. When there is a crack in the cortical bone microstructure, it is known to course around the osteons due to the crack amplifier characteristic of the cement line. Normally, if there were no cement line, the crack would pursue the Harversian canals due to the critical stress near these discontinuities.

In the analyses, the load is monitored exactly where the displacement is imposed in every step. All the phases of the composite are fragmented, as follow:

- Red HAR elements: Interface between Secondary Osteons elements;
- Light Blue HAR elements: Interface between Interstitial Matrix;
- Yellow HAR elements: Interface between Secondary Osteons and Interstitial Matrix.

3.3 One osteon bending test

The model has initially a linear relation between the force and displacement, until a crack appears near the notch at mid span. A small crack reaches the cement line before step 900 and it gradually enlarges (Fig. 7). At step 1122, the force reaches the peak value (4,74 N), and then, the reaction force decreases, while the crack coursing around the osteon through the cement line (Fig. 8). Differently from the original work of Marco et al. [5], the osteon, progressively, detaches from the interstitial matrix from both sides.

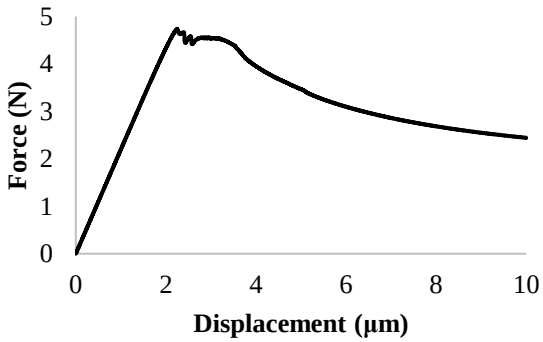

Figure 6. Force-Displacement curve of the one osteon bending test. The peak load (4,74N) is reached at step 1122 for a corresponding displacement of 2,244μm.

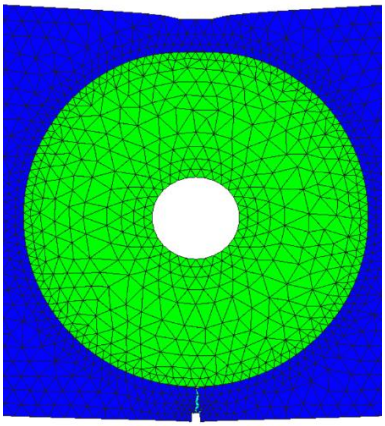

Figure 7. Step 1100. The crack reaches the cement line before step 900 and it remains restricted near the notch until the step 1122, in which the peak load (4,74N) is reached (displacements are 10 times magnified).

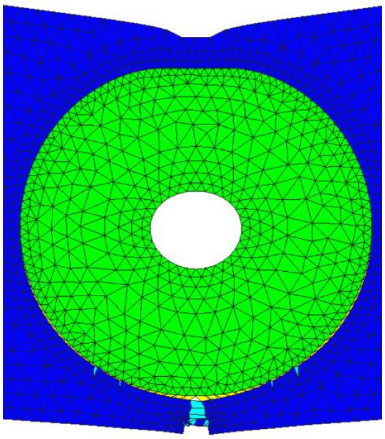

Figure 8. Step 1200. After the peak load, the crack courses around the osteon, through the cement line on both sides almost symmetrically, reaching the half of the model's height. On the side where the horizontal displacement is not restricted (right side), the crack is more noticeable (displacements are 20 times magnified).

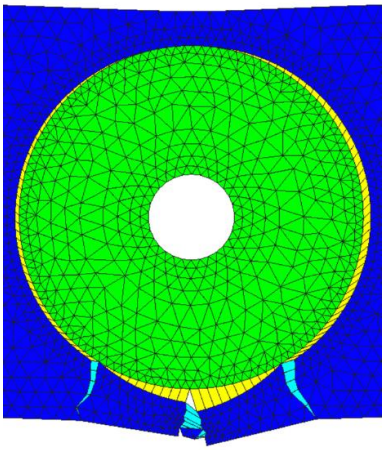

Figure 9. Crack pattern at step 5000 (displacements are not magnified).

As can be seen in Figure 9, at the end of the analysis, the osteon is almost fully disconnected from the interstitial matrix and although the crack is isolating the osteon, it is still making contact at the bottom due to the expelling force coming from the prescribed displacement.

3.4 Two osteons bending test

In this second example, an important difference from the previous model is that before the crack reaches the cement line, the interface material on the right side of the large osteon, is already damaged. In Figure 10, the Force-Displacement relation remains approximately linear until the step 500 (imposed displacement of 0,826μm) (Fig. 11). Then, the loss of stiffness is associated with the connection between the crack from the interstitial matrix and the one from the large osteon (Fig. 12). At step 1500, the crack has contoured the large osteon and is starting to propagate toward the small osteon. The crack reaches the small osteon by the step 2300 (Fig. 13). Finally, the Figure 14 shows the final crack pattern.

Figure 10. Force-Displacement curve of the two osteons bending test. The peak load (3,55N) is reached at step 1357 with a corresponding displacement of 2,244μm.

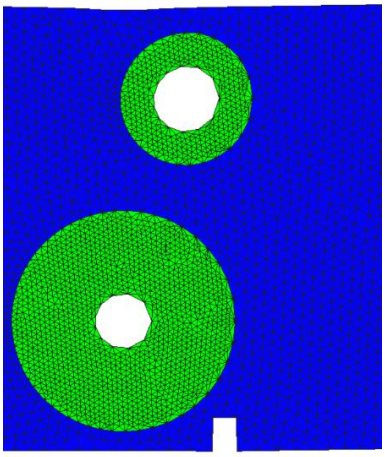

Figure 11. At step 500 (imposed displacement of 0,826μm) the model presents a linear elastic behavior (displacements are 10 times magnified).

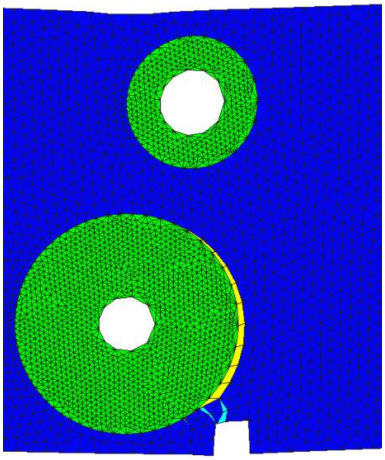

Figure 12. Approximately at step 1000 the crack reaches the cement line. (Displacements are 10 times magnified).

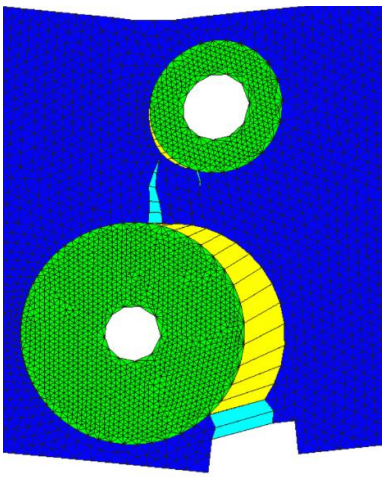

Figure 13. Approximately at step 2300, the crack reaches the top of the large osteon (displacements are 10 times magnified).

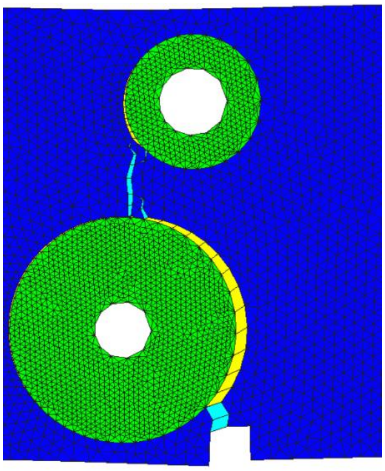

Figure 14. Crack pattern at step 5000 (displacements are not magnified).

4 Conclusions

In this work a mesh fragmentation technique based on the use of high aspect ratio (HAR) finite elements is applied to describe the crack initiation and propagation in cortical bone microstructure. The behavior of the HAR finite elements is described by a tensile-damage model. The bone is described as a 4-phased composite material (interstitial matrix, cement line, osteon and Haversian canal). The numerical model is validated through the analyses of conceptual models, as proposed by Marco et al. [5].

For both bending tests, with one and two osteons, the results obtained are in accordance with those described in literature. Different from the results obtained by Marco et al. [5], in this work, the cement line is damaged before the arrival of the crack from the matrix and, as the analysis progresses, there are more than one noticeable crack.

Finally, the results are consistent and show that the mesh fragmentation technique is a valuable approach to simulate crack propagation in cortical bone microstructure.

Acknowledgements

This study was financed in part by the Coordenação de Aperfeiçoamento de Pessoal de Nível Superior - Brasil (CAPES) - Finance Code 001.

References

[1] R. Burge; B. Dawson-Hughes; D.H. Solomon; J.B. Wong; A. King; A. Tosteson. Incidence and economic burden of osteoporosis-related fractures in the United States, 2005-2025. *Journal of bone and mineral research*, 22(3) 465-475, 2007.

[2] L. Podshivalov, A. Fischer, P.Z. Bar-Yoseph. On the road to personalized medicine: multiscale computational modeling of bone tissue. *Archives of Computational Methods in Engineering*, 21(4)399-479, 2014.

[3] L.C. Junqueira; J. Carneiro. Histologia básica. 10ª edição. *Rio de Janeiro*, 2004.

[4] E. Budyn; T.Hoc. Analysis of micro fracture in human Haversian cortical bone under transverse tension using extended physical imaging. *International Journal for Numerical Methods in Engineering*, 82(8), 940-965, 2010.

[5] M. Marco; R. Belda; M.H. Miguélez; E. Giner. A heterogeneous orientation criterion for crack modelling in cortical bone using a phantom-node approach. *Finite Elements in Analysis and Design*, 146, 107-117, 2018.

[6] A. Gustafsson; H. Khayyeri; M. Wallin; H. Isaksson. An interface damage model that captures crack propagation at the microscale in cortical bone using XFEM. *Journal of the mechanical behavior of biomedical materials*, 90, 556-565, 2019.
[7] J.G. Skedros; J.L. Holmes; E. G. Vajda; R.D. Bloebaum. Cement lines of secondary osteons in human bone are not mineral-deficient: New data in a historical perspective. *The Anatomical Record Part A: Discoveries in Molecular, Cellular, and Evolutionary Biology: An Official Publication of the American Association of Anatomists*, *286*(1), 781-803, 2005.
[8] M. M. Milovanović; J.M. Andrić; V. Medaković; J.P. Đukić; S. Zarić. Supplementary data for the article: Milovanović, MM; Andrić, JM; Medaković, VB; Djukic, J.-P.; Zarić, SD Investigation of Interactions in Lewis Pairs between Phosphines and Boranes by Analyzing Crystal Structures from the Cambridge Structural Database. Acta Crystallographica Section B: Structural Science, Crystal Engineering and Materials 2018, 74(3), 255-263, 2018. https://doi. org/10.1107/S2052520618003736. *ACTA CRYSTALLOGRAPHICA SECTION B-STRUCTURAL SCIENCE CRYSTAL ENGINEERING AND MATERIALS*.
[9] S. Nobakhti; G. Limbert; P.J. Thurner. Cement lines and interlamellar areas in compact bone as strain amplifiers-Contributors to elasticity, fracture toughness and mechanotransduction. *Journal of the mechanical behavior of biomedical materials*, *29*, 235-251, 2014.
[10] W.A.M. Brekelmans; H.W. Poort; T.J.J.H. Slooff. A new method to analyse the mechanical behaviour of skeletal parts. *Acta Orthopaedica Scandinavica*, 43(5), 301-317, 1972.
[11] R. Huiskes; E.Y. Chao. A survey of finite element analysis in orthopedic biomechanics: the first decade. *Journal of biomechanics*, 16(6), 385-409, 1983.
[12] G.N. Duda; M. Heller; J. Albinger; O. Schulz; E. Schneider; L. Claes. Influence of muscle forces on femoral strain distribution. *Journal of biomechanics*, 31(9), 841-846, 1998.
[13] M. Bessho; I. Ohnishi; J. Matsuyama; T. Matsumoto; K. Imai; K. Nakamura. Prediction of strength and strain of the proximal femur by a CT-based finite element method. *Journal of biomechanics*, 40(8), 1745-1753, 2007.
[14] P.K. Zysset; E. Dall'Ara; P. Varga; D.H. Pahr. Finite element analysis for prediction of bone strength. *BoneKEy reports*, 2, 2013.
[15] S. Li; A. Abdel-Wahab; E. Demirci; V.V. Silberschmidt. Fracture process in cortical bone: X-FEM analysis of microstructured models. Springer, Cham. In *Fracture Phenomena in Nature and Technology*, 43-55, 2014.
[16] A. Gustafsson; M. Wallin; H. Khayyeri; H. Isaksson. Crack propagation in cortical bone is affected by the characteristics of the cement line: a parameter study using an XFEM interface damage model. *Biomechanics and modeling in mechanobiology*, 1-15, 2019.
[17] D.B. Burr; M.B. Schaffler; R.G. Frederickson. Composition of the cement line and its possible mechanical role as a local interface in human compact bone. *Journal of biomechanics*, 21(11), 939-945, 1988.
[18] A.A. Abdel-Wahab; A.R. Maligno; V.V. Silberschmidt. Micro-scale modelling of bovine cortical bone fracture: Analysis of crack propagation and microstructure using X-FEM. *Computational Materials Science*, 52(1), 128-135, 2012.
[19] R. Baptista; A. Almeida; V. Infante. Micro-crack propagation on a biomimetic bone like composite material studied with the extended finite element method. *Procedia Structural Integrity*, 1, 18-25, 2016.
[20] O.L. Manzoli, M.A. Maedo, L.A.G. Bitencourt Jr.; E.A. Rodrigues. On the use of finite elements with a high aspect ratio for modeling cracks in quasi-brittle materials. *Engineering Fracture Mechanics*, 153, 151-170, 2016.
[21] O.L. Manzoli; A.L. Gamino; E.A. Rodrigues; G.K.S. Claro. Modeling of interfaces in two-dimensional problems using solid finite elements with high aspect ratio. *Computers & Structures*, 94, 70-82, 2012.
[22] J. Oliver; A.E. Huespe; S. Blanco; D.L. Linero. Stability and robustness issues in numerical modeling of material failure with the strong discontinuity approach. *Computer Methods in Applied Mechanics and Engineering*, 195(52), 7093-7114, 2006.
[23] E.A. Rodrigues; O.L. Manzoli; L.A. Bitencourt Jr; T.N. Bittencourt. 2D mesoscale model for concrete based on the use of interface element with a high aspect ratio. *International Journal of Solids and Structures*, 94, 112-124, 2016.

[24] A. Vercher; E. Giner; C. Arango; J.E. Tarancón; F.J. Fuenmayor. Homogenized stiffness matrices for mineralized collagen fibrils and lamellar bone using unit cell finite element models. *Biomechanics and modeling in mechanobiology*, 13(2), 437-449, 2014.
[25] S.C. Cowin, 2001. *Bone mechanics handbook*. CRC press.
[26] J.Y. Rho; J.D. Currey; P.E.T.E.R. Zioupos; G.M. Pharr. The anisotropic Young's modulus of equine secondary osteones and interstitial bone determined by nanoindentation. *Journal of Experimental Biology*, 204(10), 1775-1781, 2001.
[27] C.A. Villegas. *Study of the mechanical behavior of cortical bone microstructure by the finite element method* (Doctoral dissertation, Universitat Politècnica de València), 2016.
[28] E. Giner; R. Belda; C. Arango; A. Vercher-Martínez; J.E. Tarancón; F.J. Fuenmayor. Calculation of the critical energy release rate Gc of the cement line in cortical bone combining experimental tests and finite element models. *Engineering Fracture Mechanics*, 184, 168-182, 2017.